

# Efficient Analysis of Diffraction Grating with 10000 Random Grooves by Difference-Field Boundary Element Method

Jun-ichiro SUGISAKA<sup>†a)</sup>, Takashi YASUI<sup>†</sup>, and Koichi HIRAYAMA<sup>†</sup>, *Members*

**SUMMARY** A numerical investigation revealed the relation between the groove randomness of actual-size diffraction gratings and the diffraction efficiencies. The diffraction gratings we treat in this study have around 10000 grooves. When the illumination wavelength is 600 nm, the entire grating size becomes 16.2 mm. The simulation was performed using the difference-field boundary element method (DFBEM). The DFBEM treats the vectorial field with a small amount of memory resources as independent of the grating size. We firstly describe the applicability of DFBEM to a considerably large-sized structure; regularly aligned grooves and a random shallow-groove structure are calculated by DFBEM and compared with the results given by standard BEM and scalar-wave approximation, respectively. Finally we show the relation between the degree of randomness and the diffraction efficiencies for two orthogonal linear polarizations. The relation provides information for determining the tolerance of fabrication errors in the groove structure and measuring the structural randomness by acquiring the irradiance of the diffracted waves.

**key words:** *diffraction grating, random structure, numerical method, integral equation, boundary element method*

## 1. Introduction

Numerical simulations of diffraction gratings are important for designing and analyzing the device properties. For example, the groove shape affects the diffraction efficiency and the groove period determines the diffraction angles. Whereas most diffraction gratings are designed to have periodicity, actual gratings may not have perfect periodicity due to fabrication errors. Degradation of the groove periodicity affects the diffraction angles, diffraction efficiency, and directionality of the diffracted waves.

Currently, the simulation methods used for diffraction gratings are based on either scalar or vector diffraction theory. In the scalar diffraction theory (scalar-wave approximation), the amplitude of the wave transmitted through the grating is given by the simple product of the amplitude of the incident wave and the complex transmittance. The absolute value and argument of the transmittance are given by the refractive index of the material and the groove depths of the grating, respectively. In the transmittance just described, the complicated scattering at the sharp groove edges and multi-scattering among the grooves are not considered. The diffracted waves just outside of the grating are given by the Fresnel-Kirchhoff diffraction integral. The far field is simply given by the Fourier transform of the transmitted wave at the grating surface. However, when the depth of a sharp

groove is increased (a groove with high aspect) or the groove edges are dense (the grating period approaches the order of the wavelength), the contributions from the scattering at the edges and the multi-scattering effect cannot be ignored. Thus, the diffracted wave cannot be expressed by a simple product. Consequently, the computation results become less accurate. The scalar diffraction theory has been employed to large-sized structures, e.g., analyses of diffraction gratings [1], design of hybrid-level binary zone plates [2], and analysis of gratings with many particulate surface defects [3]. The limits of the scalar diffraction theory have also been discussed [4]–[6].

On the other hand, in the vector diffraction theory, the electromagnetic fields are determined such that they satisfy Maxwell's equations and the boundary conditions on all dielectric interfaces. Specifically, the finite-difference time-domain (FDTD) method is applied widely owing to its versatility. The FDTD method discretizes the entire analytical region using Yee's cells to perform numerical differentiation, and provides rigorous vectorial fields in the time domain.

The rigorous coupled wave analysis (also called the Fourier modal method) discretizes the field and dielectric structure in the wavenumber domain. This is suitable for analyses of the steady state of a periodic structure.

The fast multipole method (FMM) [7] is another direction taken for large-sized structures and many-body problems. This approach has been applied to a variety of problems, achieving simulations with low computational costs [8].

So far, many approaches have been employed for a variety of groove structures that require rigorous simulation result. Lamellar gratings with some defects illuminated by line light sources near the defect have been solved in the spectral (wavenumber) domain [9]. Gratings with up to 512 fluctuated grooves have been computed using the boundary element method (BEM) and FMM [10]. Ergül solved the scattered wave from a two-dimensional array of a large number of dielectric cubes by using FMM [11]. Random gratings expressed by super-cells having 24 or 48 grooves have been computed by the finite element method [12]. Aperiodic gratings have been designed by using FDTD simulations [13]–[15]. The FDTD method has also been applied to the random grating in a super-cell [16]. An arranged Fourier modal method for aperiodic structures has been proposed [17], [18]. The total integrated scattering formula [19] and the Monte Carlo method [20] have been used to calcu-

Manuscript received April 6, 2016.

<sup>†</sup>The authors are with Kitami Institute of Technology, Kitami-shi, 090–8507 Japan.

a) E-mail: sugisaka@mail.kitami-it.ac.jp

DOI: 10.1587/transele.E100.C.27

late a rough grating. Two-dimensional random gratings have been calculated by using the transfer-matrix method [21]. Scattering and surface plasmon polariton modes on a rough surface have been solved by using integral equations [22]. BEM has also been applied to the analyses of diffraction lenses [23] and finite-size gratings [24].

Whereas the methods described above provide rigorous results, the computational cost to calculate the whole grating device becomes considerably expensive. Actually, the electromagnetic fields of the visible light around the gratings must be discretized with intervals of submicron size, but the incident wave illuminates the grating over areas tens of millimeters wide. It is very difficult to reserve memory for this computation with a small-scale environment such as desktop computers and small-scale workstations.

In this paper, we realize a simulation for large-sized gratings with 10000 random grooves of wavelength-sized period with reduced computational costs. The simulation method is the difference-field boundary element method (DFBEM) [25], which is based on vector diffraction theory. DFBEM provides the scattered waves of locally deformed gratings; the electromagnetic field of the non-deformed grating or dielectric surface is calculated first and then the field is updated to that after deformation by solving a set of boundary-integral equations. The set of equations is at a small scale, which consists of path integrals on the boundaries around the deformed areas only. Thus, the necessary amount of memory does not depend on the whole structure size. Approximations such as truncation of the analysis region and introduction of artificial periodicity (super-cells) are not necessary. Therefore, there is no undesired scattering from the truncated edges, variation of the results among samples with the same degree of randomness, or discrete far-field effects due to the super-cells. Up to now, DFBEM has been employed for designing diffraction lenses [26] and analyzing various type of defective gratings [27], [28].

In Sec. 2, we describe the definition and quantification of the groove randomness. The condition for illumination is also presented and will be modeled in the numerical simulation.

In the calculation of random-groove gratings, we start with the reflected and transmitted wave of the dielectric plane, and then update the scattered wave by deforming the plane to add one groove. These groove-addition and field update processes are continued sequentially until all grooves are added to the plane. This calculation process is described in Sec. 3.

Before analyzing the random-groove gratings, the validity of this calculation process has to be established. For example, the result is invalid if the calculation error is accumulated in the diffracted wave through the groove-addition process. In Sec. 4, to validate the calculation process, we first describe the result of DFBEM for periodically aligned 10001 grooves. The result is then compared with that of an infinite grating computed by conventional BEM with Bloch's boundary condition. Second, we describe the analysis of a random-groove grating with 10000 low-aspect-ratio

grooves. This result is compared with that of a calculation in the scalar-wave approximation.

In Sec. 5, we describe the result for several random-groove gratings. Finally, we show the result for the dependence of the diffraction efficiency on the degree of randomness.

## 2. Structure of Random Groove Grating and Illumination Setup

The diffraction gratings treated in this paper are one-dimensional surface-relief gratings, which consist of  $N$  grooves on the surface. The grating period  $T$ , which is the distance from the center of one groove to that of the neighboring one, is constant. We fixed  $T$  to  $2.7\lambda$  throughout this paper, where  $\lambda$  is the wavelength of the incident wave in vacuum. The groove depths in the grating are considered constant,  $h$ . The groove widths in the diffraction grating are distributed normally, with an average groove width of  $0.5T$  and the variance of the distribution  $\sigma^2$  altered depending on the calculation purpose. Hereafter, we express the grating randomness by  $\sigma$ . The width of any particular groove is assumed uniform along its entire length.

The cross section of the groove is located in the  $x-y$  plane, so that the grating surface is in the  $x-z$  plane and the grooves are parallel to the  $z$  axis. The grooves on the grating are labeled  $g_n$  ( $1 \leq n \leq N$ ). The incident wave illuminates from the  $+y$  direction. In Fig. 1 (a), we depict some cross sections of the gratings with  $\sigma = 0, 0.06T$ , and  $0.12T$ . The histograms of the groove width for  $\sigma = 0.06T$  and  $0.12T$  ( $N = 10000$ ) are shown in Fig. 1 (b).

We assume that the illuminated wave is a Gaussian

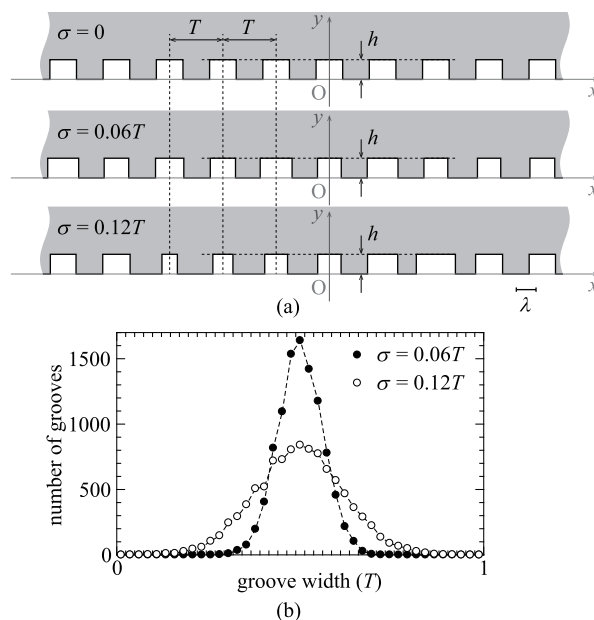


**Fig. 1** (a) Cross section of a random-groove grating for  $\sigma = 0, 0.06T$ , and  $0.12T$ . (b) Histograms of the groove width for  $\sigma = 0.06T$  and  $0.12T$ , when the number of grooves is 10000.

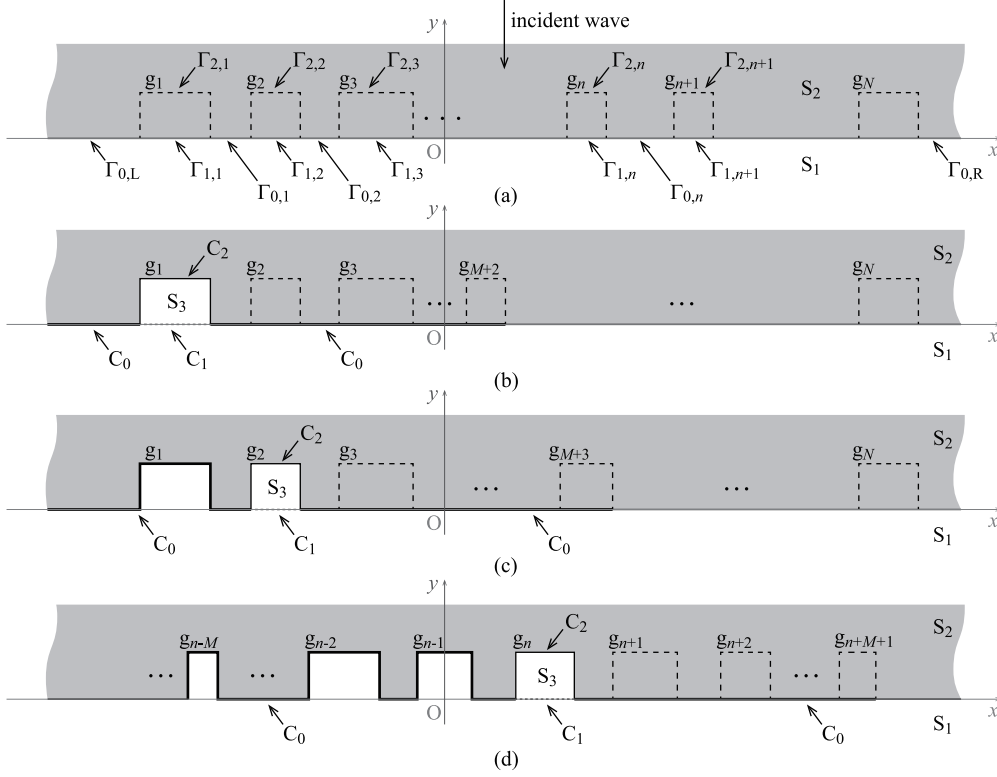


**Fig. 2** Calculation process for random groove structure with DFBEM. (a) Original structure with no groove. (b) First step: add the left edge groove  $g_1$ . (c) Second step: add the groove  $g_2$ . (d)  $n$ -th step: add the groove  $g_n$ .

beam. The beam is linearly polarized; we define the  $s$ -polarization as the electric field parallel to the groove orientation and the  $p$ -polarization as the magnetic field parallel to the groove orientation. The incident wave propagates perpendicular to the grating surface, impinging on the backside of the grating surface. It is then diffracted by the grooves on the front side.

### 3. DFBEM for Large-Sized Random-Groove Grating

This section describes the DFBEM groove addition and field update process.

First, we compute the field for a flat substrate with no grooves on it (Fig. 2 (a)). This process is called step 0. For this calculation, only the  $z$ -component of the electric field is needed for  $s$ -polarization or the  $z$ -component of the magnetic field for  $p$ -polarization. This necessary component is labeled  $f_1$  outside the substrate and  $f_2$  inside the substrate. We assume that the beam waist of the incident Gaussian beam is at the grating surface ( $y = 0$ ), that the beam width is sufficiently larger than the wavelength, and that the incident beam propagates parallel to the  $y$  axis. DFBEM requires the field at the flat substrate in the vicinity of the substrate surface,  $0 \leq y \leq h$ . The field distribution of the incident Gaussian beam around the surface (labeled  $f_i$ ) is expressed by the multiplication of a plane wave and a Gaussian window function as

$$f_i(\boldsymbol{\rho}) = e^{-ax^2} e^{jk_2y}, \quad (1)$$

and thus  $f_1$  and  $f_2$  in the vicinity of the substrate surface are written as

$$f_1(\boldsymbol{\rho}) = te^{-ax^2} e^{jk_1y}, \quad (2)$$

$$f_2(\boldsymbol{\rho}) = re^{-ax^2} e^{-jk_2y} + e^{-ax^2} e^{jk_2y}, \quad (3)$$

where  $\boldsymbol{\rho}$  is a vector that defines a position in the  $x-y$  plane. The position is also expressed by the variables  $x$  and  $y$ . Here,  $k_1$  and  $k_2$  are the wavenumbers outside and inside the substrate, respectively, whereas  $t$  and  $r$  are the transmittance and reflectance, respectively, at the substrate surface. We obtain the  $t$  and  $r$  values by approximating  $f_i(\boldsymbol{\rho}) = \exp(jk_2y)$  and using Fresnel's equations.  $a$  is determined by the beam width  $w$  (full width at half maximum) as

$$a = \frac{4 \ln 2}{w^2}. \quad (4)$$

We set  $w$  to 1/5 of the grating size. For example, when the number of grooves is 10000,  $w = 2000T$ . A set of observation points, i.e., a set of positions where we intend to find the field, is denoted by  $P = \{r_i | i = 1, 2, \dots\}$ , where  $r_i$  indicates either a position in the  $x-y$  plane or a direction of the far field. At step 0, the fields at  $P$  are given by Eqs. (2) or (3).

For the following process, we label the boundaries;  $\Gamma_{0,L}$  (infinite boundary) on the substrate at the left side of the left-edge groove  $g_1$ ,  $\Gamma_{0,R}$  (infinite boundary) on the substrate at

the right side of the right-edge groove  $\mathbf{g}_N$ ,  $\Gamma_{0,n}$  on the substrate between  $\mathbf{g}_n$  and  $\mathbf{g}_{n+1}$ , and  $\Gamma_{1,n}$  and  $\Gamma_{2,n}$  on the perimeter of  $\mathbf{g}_n$  (see Fig. 2 (a)).

Next, a groove  $\mathbf{g}_1$  is added to the flat substrate at the left edge of the grating (Fig. 2 (b)). This process is called step 1. Three regions  $S_1$ ,  $S_2$ , and  $S_3$  are defined as the region outside the substrate, inside the grating, and inside  $\mathbf{g}_1$ , respectively. The field on the boundaries, after adding the projection, is given by solving the following integral equations [27]:

$$\frac{1}{2}\Delta f_1(\boldsymbol{\rho}) = \mathcal{I}_{1,2}^{C_0}\Delta f_1 + \mathcal{I}'_{1,3}^{C_1}f_3 - \mathcal{I}_{1,2}^{C_1}f_1 \quad (\boldsymbol{\rho} \in C_0), \quad (5)$$

$$\begin{aligned} \frac{1}{2}f_3(\boldsymbol{\rho}) - \frac{1}{2}f_1(\boldsymbol{\rho}) \\ = \mathcal{I}_{1,2}^{C_0}\Delta f_1 + \mathcal{I}'_{1,3}^{C_1}f_3 - \mathcal{I}_{1,2}^{C_1}f_1 \quad (\boldsymbol{\rho} \in C_1), \end{aligned} \quad (6)$$

$$\frac{1}{2}\Delta f_1(\boldsymbol{\rho}) = -\mathcal{I}'_{2,1}^{C_0}\Delta f_1 - \mathcal{I}'_{2,3}^{C_2}f_3 + \mathcal{I}'_{2,1}^{C_1}f_1 \quad (\boldsymbol{\rho} \in C_0), \quad (7)$$

$$\begin{aligned} \frac{1}{2}f_3(\boldsymbol{\rho}) - f_2(\boldsymbol{\rho}) \\ = -\mathcal{I}'_{2,1}^{C_0}\Delta f_1 - \mathcal{I}'_{2,3}^{C_2}f_3 + \mathcal{I}'_{2,1}^{C_1}f_1 \quad (\boldsymbol{\rho} \in C_2). \end{aligned} \quad (8)$$

$$\frac{1}{2}f_3(\boldsymbol{\rho}) = -\mathcal{I}_{3,1}^{C_1}f_3 + \mathcal{I}_{3,2}^{C_2}f_3 \quad (\boldsymbol{\rho} \in C_1), \quad (9)$$

$$\frac{1}{2}f_3(\boldsymbol{\rho}) = -\mathcal{I}_{3,1}^{C_1}f_3 + \mathcal{I}_{3,2}^{C_2}f_3 \quad (\boldsymbol{\rho} \in C_2), \quad (10)$$

where the integral paths  $C_0$ ,  $C_1$ , and  $C_2$  are the boundaries defined as

$$\begin{aligned} C_0 \equiv \Gamma_{0,L} \cup (\Gamma_{0,1} \cup \Gamma_{0,2} \cup \cdots \cup \Gamma_{0,M+1}) \\ \cup (\Gamma_{1,2} \cup \Gamma_{1,3} \cup \cdots \cup \Gamma_{1,M+2}), \end{aligned} \quad (11)$$

$$C_1 \equiv \Gamma_{1,1}, \quad (12)$$

$$C_2 \equiv \Gamma_{2,1}. \quad (13)$$

The infinite path  $\Gamma_{0,L}$  at the left side of  $\mathbf{g}_1$  is truncated so that the length is equal to that of the right side of  $\mathbf{g}_1$ ,  $(\Gamma_{0,1} \cup \Gamma_{0,2} \cup \cdots \cup \Gamma_{0,M+1}) \cup (\Gamma_{1,2} \cup \Gamma_{1,3} \cup \cdots \cup \Gamma_{1,M+2})$ . The parameter  $M$  means that the integral equations contain the interaction (multi-scattering) between neighboring  $M$  grooves. For example, as  $M$  increases, the computation accuracy is improved, but more computation resources are necessary, because  $C_0$  must be extended to include the far groove  $\mathbf{g}_{M+2}$ . The number  $M$  must be set in consideration of the trade-off between the computation accuracy and the amount of computation resources. Operators  $\mathcal{I}$  and  $\mathcal{I}'$  represent the boundary integrals defined by

$$\mathcal{I}_{p,q}^C f \equiv \int_C \left\{ G_p(\boldsymbol{\rho}; \boldsymbol{\rho}') \frac{\partial f(\boldsymbol{\rho}')}{\partial n'} - f(\boldsymbol{\rho}') \frac{\partial G_p(\boldsymbol{\rho}; \boldsymbol{\rho}')}{\partial n'} \right\} dl', \quad (14)$$

$$\mathcal{I}'_{p,q} f \equiv \int_C \left\{ G_p(\boldsymbol{\rho}; \boldsymbol{\rho}') \frac{\eta_p}{\eta_q} \frac{\partial f(\boldsymbol{\rho}')}{\partial n'} - f(\boldsymbol{\rho}') \frac{\partial G_p(\boldsymbol{\rho}; \boldsymbol{\rho}')}{\partial n'} \right\} dl'. \quad (15)$$

Note that  $\mathcal{I}_{p,q}^C f$  becomes a function of  $\boldsymbol{\rho}$ . Here,  $(l, n, z)$  is a local coordinate system;  $l$  is parallel to the direction of the path integrals,  $n$  is a normal direction, and  $z$  is same as the  $z$  component of the global  $(x, y, z)$  coordinate system. The

material parameter  $\eta_i$  exhibits the magnetic permittivity in  $S_i$  for the  $s$ -polarized incident wave and electric permittivity in  $S_i$  for the  $p$ -polarized one.  $G_i$  is a free-space Green's function for  $S_i$ ;

$$G_i(\boldsymbol{\rho}; \boldsymbol{\rho}') = -\frac{j}{4} H_0^{(2)} \left( \frac{2\pi n_i}{\lambda} |\boldsymbol{\rho}' - \boldsymbol{\rho}| \right), \quad (16)$$

where  $H_0^{(2)}$  is a zero-order Hankel function of the second kind and  $n_i$  is the refractive index in the region  $S_p$  ( $p = 1, 2, 3$ ).

By discretizing  $C_0$ ,  $C_1$ , and  $C_2$  with boundary elements, the integral equations (5)–(10) are transformed to a set of simultaneous equations and solved numerically. This discretization process is the same as for the standard BEM [29]. The constant terms of the equation consist of  $f_1$  and  $\partial f_1/\partial n$  on  $C_1$  and  $f_2$  on  $C_2$ . These values are given by Eqs. (2) and (3). The solution of Eqs. (5)–(10) contains  $\Delta f_1$  and  $\partial \Delta f_1/\partial n$  on  $C_0$ , as well as  $f_3$  and  $\partial f_3/\partial n$  on  $C_1$  and  $C_2$ . From these solutions, we obtain the field after adding  $\mathbf{g}_1$  as  $f_1 + \Delta f_1$  for  $C_0$ ,  $f_3$  for  $C_1$  and  $C_2$ . The fields at  $P$  are given by adding

$$\Delta f_1(\boldsymbol{\rho}) = \mathcal{I}_{1,2}^{C_0}\Delta f_1 + \mathcal{I}'_{1,3}^{C_1}f_3 - \mathcal{I}_{1,2}^{C_1}f_1 \quad (\boldsymbol{\rho} \in S_1), \quad (17)$$

$$\Delta f_2(\boldsymbol{\rho}) = -\mathcal{I}'_{2,1}^{C_0}\Delta f_1 - \mathcal{I}'_{2,3}^{C_2}f_3 + \mathcal{I}'_{2,1}^{C_1}f_1 \quad (\boldsymbol{\rho} \in S_2), \quad (18)$$

to  $f_1$  and  $f_2$  for inside  $S_1$  and  $S_2$ , respectively, and replacing with

$$f_3(\boldsymbol{\rho}) = -\mathcal{I}_{3,1}^{C_1}f_3 + \mathcal{I}_{3,2}^{C_2}f_3 \quad (\boldsymbol{\rho} \in S_3) \quad (19)$$

for inside  $S_3$ . When a component of  $P$  is a direction of the far field, we replace  $\mathcal{I}$  and  $\mathcal{I}'$  in Eqs. (17) and (18) by the integral operators  $\mathcal{I}^{(\text{far})}$  and  $\mathcal{I}'^{(\text{far})}$ , respectively. They are defined by

$$\mathcal{I}_{p,q}^{(\text{far})C} f \equiv \frac{j}{4} \int_C \left\{ \frac{\partial f(\boldsymbol{\rho}')}{\partial n'} - jk_p (\mathbf{i}_{n'} \cdot \mathbf{i}_o) f(\boldsymbol{\rho}') \right\} e^{j\boldsymbol{\rho}' \cdot \mathbf{i}_o} dl', \quad (20)$$

$$\mathcal{I}'_{p,q}^{(\text{far})C} f \equiv \frac{j}{4} \int_C \left\{ \frac{\eta_p}{\eta_q} \frac{\partial f(\boldsymbol{\rho}')}{\partial n'} - jk_p (\mathbf{i}_{n'} \cdot \mathbf{i}_o) f(\boldsymbol{\rho}') \right\} e^{j\boldsymbol{\rho}' \cdot \mathbf{i}_o} dl'. \quad (21)$$

Note that  $\mathcal{I}_{p,q}^{(\text{far})C} f$  is a function of  $\mathbf{i}_o$ , where  $\mathbf{i}_o$  is a unit vector having the direction of the observation angle and  $\mathbf{i}_{n'}$  a unit normal vector at  $\boldsymbol{\rho}'$  on the integral path  $C$ .

In addition to  $P$ , the computation of  $f_1 + \Delta f_1$  and  $\partial(f_1 + \Delta f_1)/\partial n$  on  $\Gamma_{1,n}$  and  $f_2 + \Delta f_2$  on  $\Gamma_{2,n}$  ( $n = 2, 3, \dots, M+1$ ) are necessary for the sake of the following processes. The difference field  $\Delta f_1$  for the former is included in the solution of the integral equations and  $\Delta f_2$  for the latter is given by Eq. (18).  $\Delta f_1$  on  $\Gamma_{1,m}$  and  $\Gamma_{0,m}$  ( $m > 1 + M$ ) and  $\Delta f_2$  on  $\Gamma_{2,m}$  ( $m > 1 + M$ ) are approximated by zero. Before adding the next groove, the fields  $f_1 + \Delta f_1$ ,  $f_2 + \Delta f_2$ , and  $f_3$  are relabeled as  $f_1$ ,  $f_2$ , and  $f_1$ , respectively. We relabel  $f_3$  to  $f_1$  because the region  $S_3$  (inside  $\mathbf{g}_1$ ) at step 1 is redefined as a part of  $S_1$  in the following steps.

Second, we add the groove  $\mathbf{g}_2$  and update the field (step 2). In this step, the paths and regions are redefined as shown

in Fig. 2 (c), namely the paths  $C_0$ ,  $C_1$ , and  $C_2$  are

$$C_0 \equiv \Gamma_{0,L} \cup \Gamma_{2,1} \cup \Gamma_{0,1} \cup (\Gamma_{0,2} \cup \Gamma_{0,3} \cup \cdots \cup \Gamma_{0,M+2}) \\ \cup (\Gamma_{1,3} \cup \Gamma_{1,4} \cup \cdots \cup \Gamma_{1,M+3}), \quad (22)$$

$$C_1 \equiv \Gamma_{1,2}, \quad (23)$$

$$C_2 \equiv \Gamma_{2,2}. \quad (24)$$

The integral path  $\Gamma_{0,L}$  is truncated so that the length of  $\Gamma_{0,L} \cup \Gamma_{2,1} \cup \Gamma_{0,1}$  is equal to that of the left side of  $C_0$ ,  $(\Gamma_{0,2} \cup \Gamma_{0,3} \cup \cdots \cup \Gamma_{0,M+2}) \cup (\Gamma_{1,3} \cup \Gamma_{1,4} \cup \cdots \cup \Gamma_{1,M+2})$ .  $S_1$  is the sum of the region inside the already added groove  $g_1$  and outside of the grating, whereas  $S_3$  is inside the groove  $g_2$ . The integral equations (5)–(10) are solved with the paths described above. The constant term consists of  $f_1$  and  $\partial f_1 / \partial n$  on  $C_1$  and  $f_2$  on  $C_2$ . They have been given in step 1 as the field on  $\Gamma_{1,2}$  and  $\Gamma_{2,2}$ . The fields at  $P$  are updated by using the integral equations (17)–(19) as well as step 1. In addition to the update of  $P$ , it is necessary to compute  $f_1 + \Delta f_1$  and  $\partial(f_1 + \Delta f_1) / \partial n$  on  $\Gamma_{1,m}$  ( $3 \leq m \leq M + 2$ ) and  $f_2 + \Delta f_2$  on  $\Gamma_{2,m}$  ( $3 \leq m \leq M + 2$ ) for the sake of the following processes. After that, the fields  $f_1 + \Delta f_1$ ,  $f_2 + \Delta f_2$ , and  $f_3$  are relabeled  $f_1$ ,  $f_2$ , and  $f_3$ , respectively.

Generally, when adding a groove  $g_n$ , as shown in Fig. 2 (d), we define the integral paths as

$$C_0 \equiv \left[ \bigcup_{i=1}^M (\Gamma_{2,n-i} \cup \Gamma_{0,n-i}) \right] \cup \left[ \bigcup_{i=1}^{M+1} (\Gamma_{1,n+i} \cup \Gamma_{0,n+i-1}) \right], \quad (25)$$

$$C_1 \equiv \Gamma_{1,n}, \quad (26)$$

$$C_2 \equiv \Gamma_{2,n}. \quad (27)$$

If  $n \leq M$ , then a part of  $\Gamma_{0,L}$  is included in  $C_0$ . If  $n \geq N - M$ , then a part of  $\Gamma_{0,R}$  is included in  $C_0$ . In either case,  $\Gamma_{0,L}$  or  $\Gamma_{0,R}$  is truncated so that the lengths of  $C_0$  for the left and right side of  $g_n$  are equal. The regions  $S_1$ ,  $S_2$ , and  $S_3$  are defined as outside the grating and inside the already added grooves ( $g_1, g_2, \dots, g_{n-1}$ ), inside the grating substrate, and inside the groove  $g_n$ , respectively.

The groove-addition and field-update process is continued until all  $N$  grooves are added. Finally, the field at  $P$  becomes the field for the structure with  $N$  grooves.

The DFBEM algorithm is suitable for large  $N$  because the computer memory resources do not depend on  $N$ . The memory resource is consumed when solving the integral equations, setting the field at  $P$ , and the fields on  $\Gamma_{1,n}$  and  $\Gamma_{2,n}$ . The memory resource for the set of integral equations is determined by the number of unknowns, which depends on the lengths of integral paths  $C_0$ ,  $C_1$ , and  $C_2$ . The memory resource for  $P$  depends only on the number of its components  $r_i$ . It is not necessary to hold the fields on all  $\Gamma_{1,n}$  and  $\Gamma_{2,n}$  ( $n = 1, 2, \dots, N$ ) in memory at the same time. For example, the field on  $g_n$  ( $\Gamma_{1,n}$  and  $\Gamma_{2,n}$ ) before step  $n - M$  is equal to that given by Eqs. (2) and (3), because  $\Delta f_1$  and  $\Delta f_2$  on  $\Gamma_{1,n}$  and  $\Gamma_{2,n}$  from step 1 to  $n - M$  is approximated to zero. At step  $n - M$ , the memory region for  $\Gamma_{1,n}$  and  $\Gamma_{2,n}$  is allocated, and we calculate the field by using Eqs. (2) or (3). This field is updated across step  $n - M$  to  $n - 1$ , and then

used at step  $n$  as constant terms of the integral equations. After the integral equation is solved at step  $n$ , the field data is freed from the computer memory because these data are never used in step  $n + 1, n + 2, \dots, N$ . Thus, the memory for  $\Gamma_{1,n}$  and  $\Gamma_{2,n}$  is allocated only in step  $n - M$  to  $n$ . Consequently, the field that we must hold at any given time is only the perimeter of the  $M + 1$  grooves.

#### 4. Validation of 10000-Groove Computation

The first analysis for validation is through the comparison between DFBEM and the standard BEM. For DFBEM, 10001 grooves are regularly aligned with intervals of  $T (= 2.7\lambda)$  as shown in Fig. 3 (a). The width and height of each projection are  $0.5T$  and  $\lambda$ , respectively. The refractive indices inside of the grating ( $n_2$ ) and outside of grating ( $n_1$  and  $n_3$ ) were set to 1.5 and 1.0, respectively.

We expect that the field around the center of the grating surface (near  $g_{5001}$ ) is close to that of an infinite periodic grating. The infinitely periodic grating was calculated by BEM with Bloch's boundary condition [30]. The geometry of the grating is shown in Fig. 3 (b). The field on  $\Gamma_R$  is associated with that on  $\Gamma_L$  by Bloch's boundary condition. For both DFBEM and BEM, each boundary is discretized by line segments of length less than  $\lambda/10$  and the field distribution on each boundary element is expressed by a linear function [31]. We obtained the field distribution on the line  $-0.5T \leq x \leq 0.5T$  and  $y = -0.02T$  for comparison with

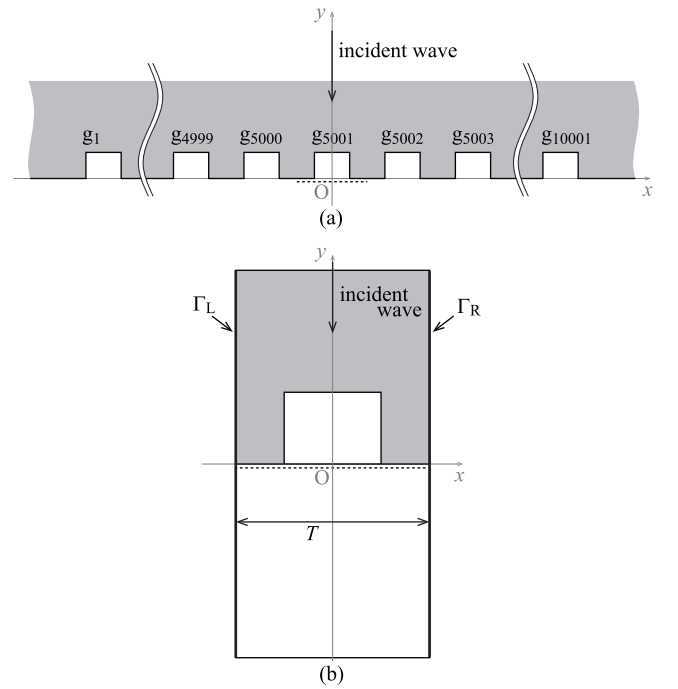


**Fig. 3** (a) Cross section of the regularly aligned 10001 grooves for calculation of DFBEM. All groove widths and depths were set constant,  $0.5T$  and  $\lambda$ , respectively. (b) Geometry for the calculation of a periodic grating with BEM. Bloch's boundary condition is applied on the left and right side boundaries  $\Gamma_L$  and  $\Gamma_R$ . The groove width and depth were also set to  $0.5T$  and  $\lambda$ , respectively.

DFBEM. The observation lines for each DFBEM and BEM simulation are indicated by dashed lines in Figs. 3 (a) and 3(b), respectively. They were regularly discretized into 41 points, which are components of the observation point set  $P$ . The calculated fields for DFBEM and BEM are denoted by  $f_i^{(\text{DFBEM})}$  and  $f_i^{(\text{BEM})}$ , respectively. The index  $i$  ( $1 \leq i \leq 41$ ) varies with the  $x$  coordinate.

By selecting the groove number as 10001, the grating center, where the  $y$ -axis and the center of the incident Gaussian beam are positioned, is at the center of  $g_{5001}$ . Because of this condition, the grating structure and the incident beam are both symmetric about the  $y$ -axis. In the condition of BEM, the grating structure and the incident beam (a plane wave propagating in the  $-y$  direction) are also both symmetric about the  $y$ -axis as shown in Fig. 3 (b). Therefore, we can expect a good agreement between the DFBEM and BEM results.

We implemented a DFBEM program that is written in Fortran 95, and compiled by using the GNU fortran compiler (GFortran). The integral equations of DFBEM were transformed to simultaneous equations, and then solved by  $LU$  decomposition with the LAPACK library. We ran the program with a desktop computer that has an Intel Core i7-5930K CPU. No parallel computing such as multicore processing, clustering, or graphical processing unit, was used in the computation.

The results (real part of the complex field) for the  $s$ - and  $p$ -polarizations are shown in Fig. 4. As we expected, the results of DFBEM is close to those of standard BEM for both polarizations. We also evaluated the average error  $e$  (%), which is defined by

$$e = \frac{100}{41} \sum_{i=1}^{41} \frac{|f_i^{(\text{DFBEM})} - f_i^{(\text{BEM})}|}{|f_i^{(\text{BEM})}|}, \quad (28)$$

and listed in Table 1.

The table indicates that the average error (computation accuracy) can be reduced by increasing  $M$ . Moreover, as described in Sect. 3, we can see the trade-off relation between the computation accuracy and the computation resources (CPU time and memory). In the following analyses, we decided to employ the setting  $M = 3$ .

In the second analysis, we confirm the reliability of the far field for the random groove structure. As we described in Sect. 1, the scalar approximation is valid for sufficiently shallow groove structures. Thus, the result of DFBEM is compared with that of the scalar approximation.

The randomness of the groove is fixed to  $\sigma = 0.14T$ , and we prepared 16 grating samples whose groove depth  $h$  was varied from  $0.03T(0.081\lambda)$  to  $0.48T(1.296\lambda)$ . The observed point set  $P$  contains two directions of  $-90^\circ$  and  $-68.2615^\circ$  for the far fields. Those are angles from the  $+x$  axis, corresponding to the zero-order and first-order diffraction angles of a diffraction grating with a  $2.7\lambda$  period.

At step 0, it is necessary to compute the far fields that belong to  $P$ . Those far fields  $f_1^{(\text{far})}(\mathbf{i}_p)$  consist of waves transmitted through the flat substrate, which is algebraically cal-

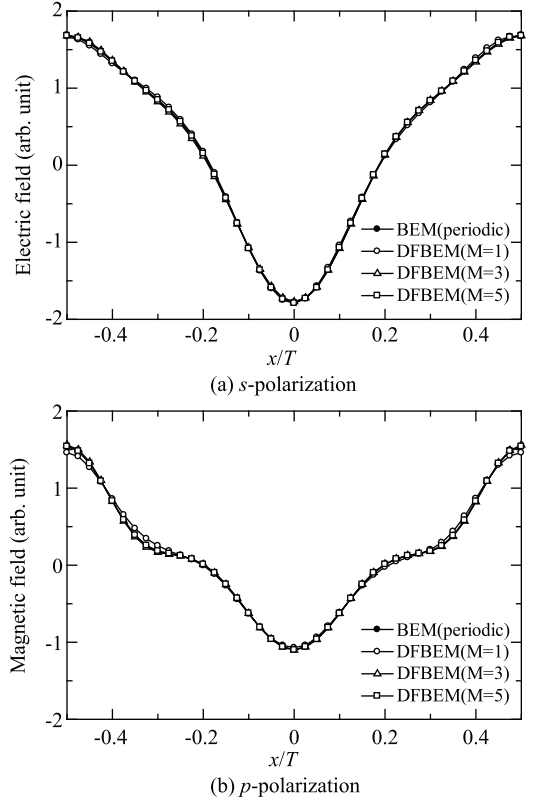


**Fig. 4** Field distribution computed by DFBEM ( $M = 1, 3$ , and  $5$ ) on the grating surface  $y = -0.02T$  and  $-T/2 \leq x \leq T/2$ . As  $M$  increases, the field distributions for both the  $s$ - and  $p$ -polarization become close to that calculated by BEM with Bloch's boundary condition (see also Table 1).

**Table 1** Average relative error  $e$  between BEM (periodic structure) and DFBEM for  $M = 1, 3$ , and  $5$ . Whereas the error reduces as  $M$  increases, the necessary calculation resources (CPU time and memory consumption) increase.

$M$	$s$ -polarization		$p$ -polarization		CPU time (h)	Memory (Mbyte)
	$e$ (%)	$e$ (%)	$e$ (%)	$e$ (%)		
1	8.09	5.13	1.721	13.66		
3	1.54	2.15	10.48	50.16		
5	0.664	0.808	30.96	110.8		

culated by

$$f_1^{(\text{far})}(\mathbf{i}_p) = \mathcal{I}_{1,1}^{(\text{far})C} f_1, \quad (29)$$

where  $f_1$  is given by Eq. (2), and  $C$  is an infinite path along the grating surface  $y = 0$ .

In the calculation under the scalar approximation, the far field is given by

$$f^{(\text{far})}(\mathbf{i}_p) = \mathcal{I}_{1,1}^{(\text{far})C} f, \quad (30)$$

where  $C$  is an integral path on  $y = 0$ . The directions of the far fields ( $\mathbf{i}_p$ ) are same as the components of  $P$  for DFBEM, namely,  $-90^\circ$  (zero-order) and  $-68.2615^\circ$  (first-order).  $f$  is the field on  $y = 0$  ( $S_1$  side), which is given by

$$f(x) = \begin{cases} te^{-ax^2} & (x \in \Gamma_{0,n}, n = 1, 2, \dots, N-1) \\ te^{-ax^2} e^{-j(k_1 - k_2)h} & (x \in \Gamma_{1,n}, n = 1, 2, \dots, N). \end{cases} \quad (31)$$

$$(32)$$

$t$  is the transmittance through the boundary from the inside to the outside of the grating, which is given by the Fresnel's equation as

$$t = \begin{cases} \frac{2k_2}{k_1 + k_2} & (s\text{-polarization}) \\ \frac{2k_2/n_2^2}{k_1/n_1^2 + k_2/n_2^2} & (p\text{-polarization}). \end{cases} \quad (33)$$

The calculation results (irradiance) for DFBEM and the

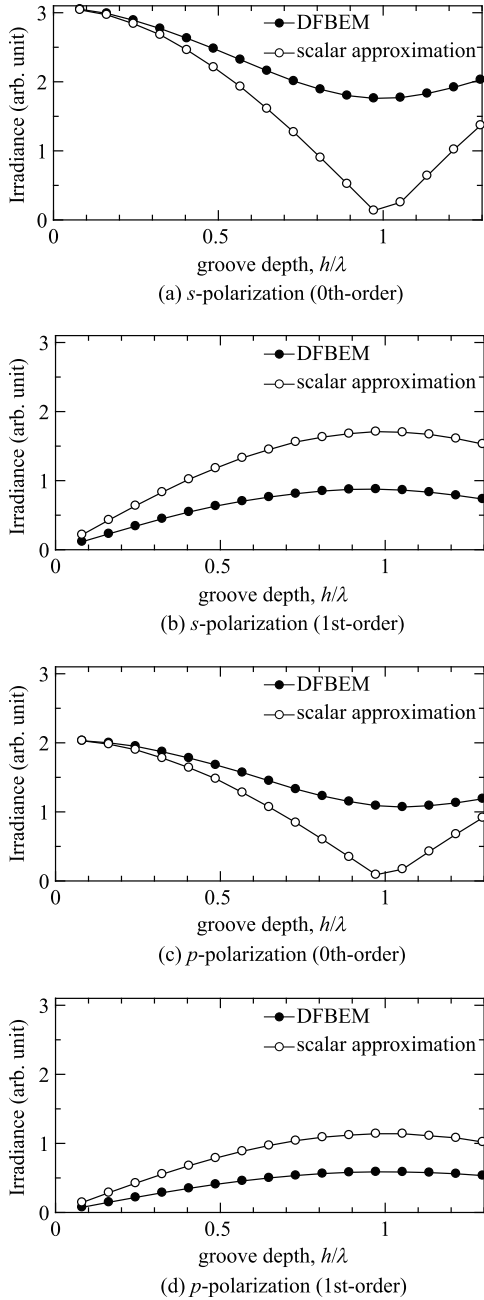


**Fig. 5** Irradiance for the zeroth and first order diffracted wave computed by DFBEM and the scalar-wave approximation. The randomness of the groove  $\sigma$  is 0.147. As the groove depth decreases, the results for DFBEM and the scalar-wave approximation are in good agreement.

scalar approximation are shown in Fig. 5. For small  $h$ , the results of DFBEM are very close to those of the scalar approximation. This result shows the validity of DFBEM for the calculation of the random groove structure and the far fields. In the scalar approximation, as we can see from Eqs. (31) and (32), the wavefronts are discontinuous at the groove edges, in violation of Maxwell's equations, because the boundary condition on the wall surface of the grooves is not considered. This discontinuity increases as the groove depths  $h$  increases. Therefore, the precision of the scalar approximation decreases as  $h$  becomes larger.

## 5. Diffraction Efficiency of Random Grooves

In this section, we describe the relation between the randomness of the grooves and the diffraction efficiency. The groove depth  $h$  was set to  $\lambda$ . The randomness of the groove width  $\sigma$  was varied from zero to 0.137. We computed the diffraction efficiency, defined by the ratio of the irradiances of the two far fields: the first-order diffracted wave toward  $-68.2615^\circ$  and that of the incident wave toward  $-90^\circ$ . The far field of the incident wave  $f_i^{(\text{far})}(\mathbf{i}_0)$  is given by

$$f_i^{(\text{far})}(\mathbf{i}_0) = \mathcal{I}_{2,2}^{(\text{far})C} f_i, \quad (35)$$

where  $\mathbf{i}_0$  is a unit vector oriented along  $-90^\circ$ .  $C$  is an infinite integral path on  $y = 0$ , and  $f_i$  is the incident wave on  $C$  given by Eq. (1). Note that this far field is calculated with the incident wave in the grating substrate after changing its amplitude by passing through the dielectric interface on the backside of the grating. Hence, the diffraction efficiency is not comparable to the experimentally acquired one, unless

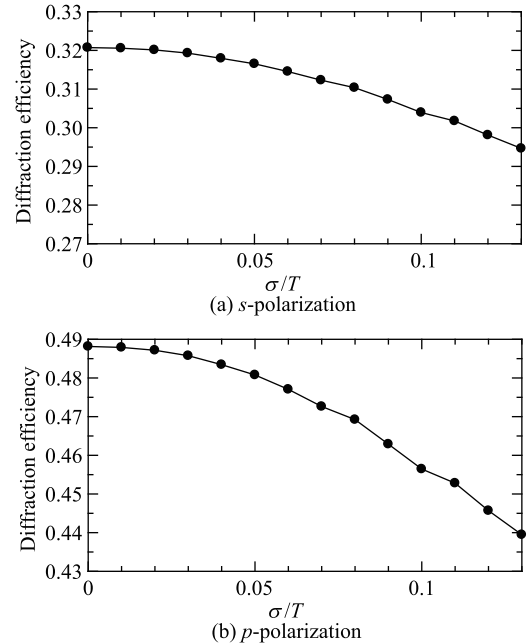


**Fig. 6** Relation between the groove randomness and the diffraction efficiency of the first order. The diffraction efficiencies for both  $s$ - and  $p$ -polarization decrease as the groove randomness increases.

**Table 2** Variation of diffraction efficiency of 12 samples having a fixed randomness  $\sigma = 0.08T$ .

sample index	<i>s</i> -polarization		<i>p</i> -polarization	
	diffraction efficiency	variation (%)	diffraction efficiency	variation (%)
1	0.3101889	0.00103	0.4687677	0.0108
2	0.3101289	0.0204	0.4688499	0.0283
3	0.3105448	0.114	0.4694407	0.154
4	0.3098147	0.122	0.4677728	0.201
5	0.3104708	0.0899	0.4695449	0.177
6	0.3106178	0.137	0.4698991	0.252
7	0.3103766	0.0595	0.4691750	0.0977
8	0.3100388	0.0494	0.4683618	0.0758
9	0.3103165	0.0401	0.4688713	0.0329
10	0.3100175	0.0563	0.4682840	0.0924
11	0.3098675	0.105	0.4677389	0.209
12	0.3099223	0.0870	0.4679009	0.174
average	0.3101921	–	0.4687173	–

the incident far field was calculated from the incident wave before entering the grating substrate.

The computation results are plotted in Fig. 6. For both *s*- and *p*-polarizations, the diffraction efficiency monotonically decreases as the randomness  $\sigma$  increases. The relation between the groove randomness and the diffraction efficiency is known qualitatively; for random grooves spacings, the scattered wave radiated from the grooves cannot be in phase in the direction of the theoretical diffraction angle. The results of Fig. 6 agree with the qualitative discussion.

The parameter  $\sigma$  is a statistical number and the diffraction efficiency may vary among the samples for the same  $\sigma$ . To investigate the range of variation, we prepared 12 groove patterns that have the same randomness  $\sigma = 0.08T$ , but created by using different random numbers. Each diffraction efficiency and the variation from the average diffraction efficiency for both *s*- and *p*-polarization is listed in Table 2.

The table shows that the variation for the *s*- and *p*-polarization are less than 0.137% and 0.252%, respectively. For smaller  $\sigma$  the variation range would be reduced, because for small  $\sigma$ , the structural variation becomes small, and at  $\sigma = 0$  the variation must be zero.

## 6. Conclusion

In this paper, we have presented the numerical analysis of the diffraction efficiencies of diffraction gratings with random grooves. The numerical method is based on DFBEM, which makes it possible to solve the scattering problem with small amount of computation resources. In the analysis of 10001 grooves, the necessary CPU time was 10.48 h, and the memory consumption was 50.16 Mbyte. Because the requisite memory size is very small, DFBEM is suitable for concurrent computation of various grating parameters. Combining this with parallel computing such as multicore CPU and graphical processing unit, the computation can be made even more efficient.

We have also validated the application of DFBEM to an extremely large-sized diffraction gratings. The field distribution of regularly aligned 10001 grooves calculated by DFBEM agreed with that calculated by BEM with Bloch's boundary condition. DFBEM was also applied to 10000

random groove structures; the results agree with that of the scalar-wave approximation for a shallow groove structure. From those analyses, we conclude that DFBEM provides reliable results for both large-sized random groove structures.

In the numerical simulation of the random diffraction gratings, the structures and the illumination setup were directly modeled after the actual case. We noticed the randomness of the groove width, and obtained a relation between the randomness and the diffraction efficiency. There is little variation among the samples with the same randomness. For this reason, the computed diffraction efficiency is a global characteristic of the grating, not determined by the local groove structure in the grating.

If we assume the wavelength 600 nm, the grating size we treated in this work is 16.2 mm, and the incident beam width is 3.24 mm. This configuration is easy to set up experimentally. Although the task to consider the reflectance and transmittance at the backside of the grating surface remains, we expect the result to become quantitatively comparable to the experimental one.

In the future, this work would be applied to the design of diffraction gratings and quality examination of produced gratings. For example, the relation between the groove randomness and the wavelength resolution can be used to estimate the tolerance for the fabrication error of products. By computing the far field distribution for several wavelengths, we can also find the wavelength resolution of the grating and its dependence on the groove randomness. As another application, by referring to the simulation result of the relation between the groove randomness and the diffraction efficiency, we can determine the groove randomness of products from a simple examination, where one illuminates the product and measures the irradiance of the first-order diffracted wave. However, actual diffraction gratings could have many kind of randomness other than in the groove width, such as randomness in period, groove depth, groove shape, and grating-surface roughness. Each randomness can be analyzed by DFBEM only if the cross sectional geometry of the grating is available. Our future work is to analyze such other types of randomness and to characterize the effect on the diffracted wave.

## References

- [1] R. Magnusson and T.K. Gaylord, "Diffraction efficiencies of thin phase gratings with arbitrary grating shape," *J. Opt. Soc. Am.*, vol.68, no.6, pp.806–809, June 1978.
- [2] Y. Orihara, W. Klaus, M. Fujino, and K. Kodate, "Optimization and application of hybrid-level binary zone plates," *Appl. Opt.*, vol.40, no.32 pp.5877–5885, Nov. 2001.
- [3] L.M. Sanchez-Brea and F.J. Torcal-Milla, "Near-field diffraction of gratings with surface defects," *Appl. Opt.*, vol.49, no.11 pp.2190–2197, April 2010.
- [4] S.D. Mellin and G.P. Nordin, "Limits of scalar diffraction theory and an iterative angular spectrum algorithm for finite aperture diffractive optical element design," *Opt. Express*, vol.8, no.13, pp.705–722, June 2001.
- [5] D. Ruan, L. Zhu, X. Jing, Y. Tian, L. Wang, and S. Jin, "Validity of scalar diffraction theory and effective medium theory for analysis of a blazed grating microstructure at oblique incidence," *Appl. Opt.*, vol.53, no.11, pp.2357–2365, April 2014.
- [6] D.A. Pommet, M.G. Moharam, and E.B. Grann, "Limits of scalar diffraction theory for diffractive phase elements," *J. Opt. Soc. Am. A*, vol.11, no.6 pp.1827–1834, Jun. 1994.
- [7] V. Rokhlin, "Rapid solution of integral equations of scattering theory in two dimensions," *J. Comput. Phys.*, vol.86, no.2, pp.414–439, Nov. 1990.
- [8] Ö. Ergül and L. Gürel, "Iterative solutions of electromagnetics problems with MLFMA," in *The multilevel fast multipole algorithm (MLFMA) for solving large-scale computational electromagnetics problems*, pp.177–268, Wiley, Piscataway, 2014.
- [9] K. Watanabe, J. Pištora, and Y. Nakatake, "Rigorous coupled-wave analysis of electromagnetic scattering from lamellar grating with defects," *Opt. Express*, vol.19, no.25 pp.25799–25811, Dec. 2011.
- [10] A. Sato, "Analysis of finite-sized guided-mode resonant gratings using the fast multipole boundary element method," *J. Opt. Soc. Am. A*, vol.27, no.9, pp.1909–1919, Sept. 2010.
- [11] Ö. Ergül, "Solutions of large-scale electromagnetics problems involving dielectric objects with the parallel multilevel fast multipole algorithm," *J. Opt. Soc. Am. A*, vol.28, no.11, pp.2261–2268, Nov. 2011.
- [12] H. Gross, M.-A. Henn, S. Heidenreich, A. Rathsfeld, and M. Bär, "Modeling of line roughness and its impact on the diffraction intensities and the reconstructed critical dimensions in scatterometry," *Appl. Opt.*, vol.51, no.30, pp.7384–7394, Oct. 2012.
- [13] T. Oonishi, T. Konishi, and K. Itoh, "Fabrication of phase only binary blazed grating with subwavelength structures designed by deterministic method based on electromagnetic analysis," *Jpn. J. Appl. Phys.*, vol.46, no.8B pp.5435–5440, Aug. 2007.
- [14] J. Ala-Laurinaho, T. Hirvonen, J. Tuovinen, and A.V. Räsänen, "Numerical modeling of a nonuniform grating with FDTD," *Microwave Opt. Tech. Lett.*, vol.15, no.3, pp.134–139, June 1997.
- [15] D. Feng, P. Ou, L.-S. Feng, S.-L. Hu, and C.-X. Zhang, "Binary sub-wavelength diffractive lenses with long focal depth and high transverse resolution," *Opt. Express*, vol.16, no.25, pp.20968–20973, Dec. 2008.
- [16] M. Hakko, T. Kiire, D. Barada, T. Yatagai, and Y. Hayasaki, "Ultra-weak background scattered light reveals structure of a diffractive element," *Opt. Lett.*, vol.38, no.19 pp.3862–3865, Oct. 2013.
- [17] E. Silberstein, P. Lalanne, J.-P. Hugonin, and Q. Cao, "Use of grating theories in integrated optics," *J. Opt. Soc. Am. A*, vol.18, no.11, pp.2865–2875, Nov. 2001.
- [18] M. Pisarenco, J.M.L. Maubach, I.D. Setija, and R.M.M. Mattheij, "Efficient solution of Maxwell's equations for geometries with repeating patterns by an exchange of discretization directions in the aperiodic Fourier modal method," *J. Comput. Phys.*, vol.231, no.24, pp.8209–8228, Aug. 2012.
- [19] P. Zhou and J. Burge, "Coupling of surface roughness to the performance of computer-generated holograms," *Appl. Opt.*, vol.46, no.26 pp.6572–6576, Sept. 2007.
- [20] P. Tran and V. Celli, "Monte Carlo calculation of backscattering enhancement for a randomly rough grating," *J. Opt. Soc. Am. A*, vol.5, no.10, pp.1635–1637, Oct. 1988.
- [21] C. Lin, N. Huang, and M.L. Povinelli, "Effect of aperiodicity on the broadband reflection of silicon nanorod structures for photovoltaics," *Opt. Express*, vol.20, no.101, pp.A125–A132, Dec. 2012.
- [22] F. Toigo, A. Marvin, V. Celli, and N.R. Hill, "Optical properties of rough surfaces: General theory and the small roughness limit," *Phys. Rev. B*, vol.15, no.12, pp.5618–5626, Jun. 1977.
- [23] E. Glytsis, M.E. Harrigan, T.K. Gaylord, and K. Hirayama, "Effects of fabrication errors on the performance of cylindrical diffractive lenses: rigorous boundary-element method and scalar approximation," *Appl. Opt.*, vol.37, no.28, pp.6591–6602, Oct. 1998.
- [24] K. Hirayama, E.N. Glytsis, and T.K. Gaylord, "Rigorous electromagnetic analysis of diffraction by finite-number-of-periods gratings," *J. Opt. Soc. Am. A*, vol.14, no.4, pp.907–917, April 1997.
- [25] J.-I. Sugisaka and T. Yatagai, "Fast and highly accurate boundary element method for scattering calculation of defective gratings," *Opt. Lett.*, vol.37, no.11, pp.2079–2081, June 2012.
- [26] J.-I. Sugisaka and T. Yatagai, "High efficient design method of large diffractive optical elements by vectorial field analysis based on boundary element method," *Proc. SPIE*, vol.8556, pp.85560T-1–85560T-13, Nov. 2012.
- [27] J.-I. Sugisaka, T. Yasui, and K. Hirayama, "Expansion of the difference-field boundary element method for numerical analyses of various local defects in periodic surface-relief structures," *J. Opt. Soc. Am. A*, vol.32, no.5, pp.751–763, May 2015.
- [28] J.-I. Sugisaka, T. Yasui, and K. Hirayama, "Efficient Scattering Analysis of Arbitrarily Shaped Local Defect in Diffraction Grating," *IEICE Trans. Electron.*, vol.E99-C, no.1, pp.76–80, Jan. 2016.
- [29] N. Morita, N. Kumagai, and J.R. Mautz, "The numerical solution of integral equations," in *Integral equation methods for electromagnetics*, pp.233–327, Artech house, Norwood, 1990.
- [30] Y. Nakata and M. Koshiba, "Boundary-element analysis of plane-wave diffraction from groove-type dielectric and metallic gratings," *J. Opt. Soc. Am. A*, vol.7, no.8, pp.1494–1502, Aug. 1990.
- [31] A. Tadeu and J. António, "Use of constant, linear and quadratic boundary elements in 3D wave diffraction analysis," *Eng. Anal. Bound. Elem.*, vol.24, no.2, pp.131–144, Feb. 2000.



**Jun-ichiro Sugisaka** received the B.E., M.E., and Ph.D. degree in optics and photonics from University of Tsukuba, Tsukuba, Japan, in 2005, 2007, and 2010, respectively. From 2008 to 2010, he was a Research Fellow of the Japan Society for the Promotion Science. From 2010 to 2013, he joined Center for Optical Research Education in Utsunomiya University, Utsunomiya, Japan as a Doctoral Research Fellow. Since then he has been an Assistant Professor of the Department of Electrical and Electronic Engineering, Kitami Institute of Technology, Kitami, Japan. His research interests are in photonic crystal, diffraction, scattering theory and their computer simulation, and works for developing integrated lightwave circuits and novel simulation algorithms. Dr. Sugisaka is a member of the Japan Society of Applied Physics, IEEE, and the Optical Society of America.



**Takashi Yasui** received the B.S. degree in electronic engineering from Fukui University, Fukui, Japan, in 1997, and the M.S. and Ph.D. degrees in electronic engineering from Hokkaido University, Sapporo, Japan, in 1999 and 2001, respectively. From 1999 to 2002, he was a Research Fellow of the Japan Society for the Promotion of Science. In 2002, he joined Fujitsu Ltd., Chiba, Japan. From 2004 to 2011, he was an Assistant Professor of the Department of Electronic and Control Systems Engineering,

Shimane University, Matsue, Japan. Since 2011, he has been an Associate Professor of the Department of Electrical and Electronic Engineering, Kitami Institute of Technology, Kitami, Japan. He has been engaged in research on wave electronics. Dr. Yasui is a member of the Applied Computational Electromagnetics Society, the Optical Society of America, IEEE, and the Magnetics Society of Japan.



**Koichi Hirayama** received the B.S., M.S., and Ph.D. degrees in electronic engineering from Hokkaido University, Sapporo, Japan, in 1984, 1986, and 1989, respectively. In 1989, he joined the Department of Electronic Engineering, Kushiro National College of Technology, Kushiro, Japan. In 1992, he became an Associate Professor of Electronic Engineering at Kitami Institute of Technology, Kitami, Japan, and in 2004 he became a Professor. He has been interested in the analysis and optimal design of

electromagnetic and optical waveguides. Dr. Hirayama is a senior member of IEEE and a member of the Japan Society of Applied Physics.